Applied Chemical Engineering (2023) Volume 6 Issue 1
doi:10.24294/ace.v6i1.1965

ORIGINAL RESEARCH ARTICLE

Complex dielectric-impedance spectroscopic studies of magnetite added chitin biopolymer

Sanjeeta Rani[1], Sunita Hooda[2], Neelu Dheer[3], V Bhasker Raj[1], Ishwar Prasad Sahu[4], Manisha Verma[1*]

[1] *Department of Physics, Acharya Narendra Dev College, University of Delhi, Govindpuri, Kalkaji, New Delhi 110019, India. E-mail: manishaverma@andc.du.ac.in*

[2] *Polymer Research Laboratory, Department of Chemistry, Acharya Narendra Dev College, University of Delhi, Govindpuri, Kalkaji, New Delhi 110019, India.*

[3] *Department of Chemistry, Acharya Narendra Dev College, University of Delhi, Govindpuri, Kalkaji, New Delhi 110019, India.*

[4] *Department of Physics, Indira Gandhi National Tribal University, Amarkantak, Madhya Pradesh 484887, India.*

ABSTRACT

We have successfully synthesized magnetic chitin (MCH) by incorporating iron oxide nanoparticles into biodegradable and abundantly naturally available chitin by the coprecipitation method. X-ray diffraction (XRD) characterization revealed formation of cubic inverse spinel structure of Fe_3O_4 nanoparticles. In addition to this, other characterization studies like energy dispersive X-ray analysis (EDX) and vibrating sample magnetometry (VSM) were also performed to have an insight into the compositional and functional nature of the structure. A detailed spectroscopic study of complex impedance and dielectric constant for a wide frequency range of ~1 Hz to 10 MHz at discrete temperatures ~300–400 K has been performed by us for the first time on MCH in order to understand various relaxation processes. From permittivity, we have estimated the height of the potential barrier to be ~95.8 ± 0.3 meV. Impedance measurements yielded an activation energy of ~35.85 meV. Thermogravimetric analysis (TGA) of the sample showed exceptionally high thermal stability of the sample with percentage of residual mass at 800 °C being ~73% in MCH, which is quite high in comparison to the pristine chitin. An *S* shaped curve obtained through VSM measurement confirmed the superparamagnetic nature of the nanocomposite. The study assumes significance in the present scenario of rising awareness about the environment and demand to explore alternative green materials with numerous biomedical/environmental applications ranging from drug delivery vehicles in COVID-19 treatment to food packaging.

Keywords: Biopolymer; Chitin; Complex Dielectric Constant; Complex Impedance; Thermal Stability; Magnetite; Nanoparticle

ARTICLE INFO

Received: 28 February 2023
Accepted: 26 April 2023
Available online: 19 May 2023

1. Introduction

The rising awareness about global environmental problems augmented by rampant usage of petroleum-based polymers has motivated researchers worldwide to create alternative green materials[1–3]. Chitin nanostructures[4,5], due to their nanosized dimensions and distinct properties, are increasingly emerging as a viable choice for the fabrication of functional bio-nanocomposite materials for use in a diverse range of applications[6] ranging from drug delivery vehicles[7] in COVID-19 treatment, wound dressings[8] to environmentally safe food packaging membranes[9]. To enhance the biocompatibility and applications of biopolymers, numerous attempts have been made, wherein biopolymers have structurally been altered by the incorporation of metal oxide nanoparticles[10], which makes them suitable for a variety of applications, including magnetically targeted cancer therapy[11] and improved targeting

of biomolecules for relevant biosensing applications[12].

Superparamagnetic Fe_3O_4 nanoparticles have recently been dispersed to enhance the optoelectrical properties of chitosan[13]: a well-known derivative of chitin, the subject of our study. Complex impedance spectroscopic studies of dielectric properties of materials provide significant information about the correlation between the electrical properties and the microstructure, specifically the grains, grain boundaries and the material-electrode interface. This information is particularly useful in optimization of design parameters for applications in a variety of domains[14].

Understanding the significance of polysaccharide-based materials in electrical applications for a variety of biological and engineering purposes requires a detailed assessment of dielectric and conductive properties[15,16]. Polymer nanocomposites are made up of nanofillers, such as carbon-based nanoparticles, ferrite, metal nanoparticles and polymers as the matrix phase[17]. In our study, we have chosen the nanoparticles doped biopolymer chitin because its fabrication is relatively inexpensive and it has adjustable electrical properties. We were successful in modifying the properties of chitin[18,19] significantly, in order to improve its electrical properties by adding nanosized magnetite particles. Characterization studies of magnetic chitin (MCH) were performed using X-ray diffraction (XRD), energy dispersive X-ray (EDX) analysis, vibrating sampling magnetisation (VSM) techniques and thermogravimetric analysis (TGA). To the best of our knowledge, the complex spectroscopic impedance and dielectric studies for magnetic chitin have not been reported so far. In the work presented here, we report the dielectric behaviour and impedance spectroscopic studies of the magnetic chitin nanocomposite material from 1 Hz to 10 MHz at certain representative temperatures in order to gain valuable insight into the underlying mechanisms of biopolymer nanocomposites.

2. Experimental details

2.1 Material and methods

Analytical grade reagents were used in the preparation of samples. Iron (III) chloride ($FeCl_3$, 96.0%), Iron (II) chloride ($FeCl_2$, 96.0%), chitin (99%) and Ammonia solution (NH_3, 25 wt.%), were purchased from Merck. MCH was prepared by the coprecipitation method[20,21].

2.2 Sample characterization

The thermogravimetric scans of the polymer nanocomposites were performed by using the TGA HiRes 1000 thermal analyzer besides XRD, VSM and EDX. The powder samples were heated in an alumina pan at 10 ℃/min from 25 ℃ to 900 ℃ in N_2 gas at the flow rate of 20 mL/min. Complex impedance spectroscopy was carried out on the Novacontrol Technology Make Dielectric/Impedance analyzer equipped with an automatic data acquisition display. The powdered sample was pelletized (thickness 1 mm; diameter 12 mm) by a hydraulic press under ~50 MPa, and well-polished using an emery paper. The pellet was coated by a thin and uniform layer of silver paste to study the dielectric and impedance properties in the frequency range of 1 Hz to 10 MHz from 300 K to 400 K under a DC bias voltage of 1 V.

2.3 Synthesis of MCH

4 mL each of 0.5 M $FeCl_3$ and 0.25 M $FeCl_2$ were mixed and agitated for 20 minutes at room temperature. A yellow colored solution was obtained on adding CH which changed into a brownish black precipitate on the addition of NH_3 solution. This black precipitate was washed and vacuum dried at 40 ℃ for a day to finally get a dark brown powder.

3. Results and discussion

3.1 XRD analysis

In conformity with JCPDS CARD 19-0629, the characteristic peaks of Fe_3O_4 nanoparticles[22,23] appear at 35.60°, 43.10°, 57.36° and 62.82° corresponding to (311), (400), (422) and (440) planes of pure Fe_3O_4 in MCH nanocomposites (**Figure 1**). This confirms the successful incorporation of magnetite nanoparticles onto pristine CH. Additionally, the characteristic peak of CH at $2\theta = 9.10°$ and 22.94° can also be seen in our sample. Elsayed *et al.*[24] have also reported similar behaviour in their sample. The size of the Fe_3O_4 nanoparticles quantitatively evaluated from the major diffraction peak of (311) using Debye–Scherrer equation[25] was estimated to be 25 nm.

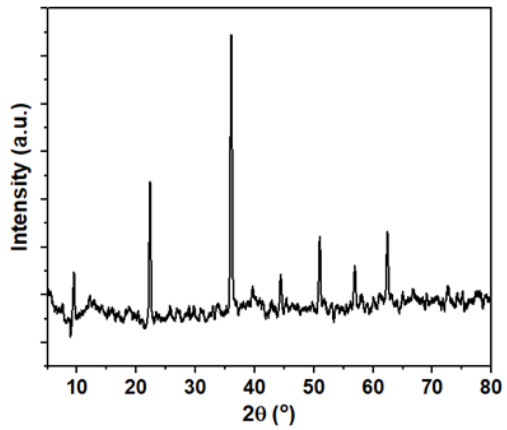

Figure 1. X-ray diffraction pattern of MCH, showing peaks of Fe_3O_4 and pristine CH.

3.2 EDX analysis

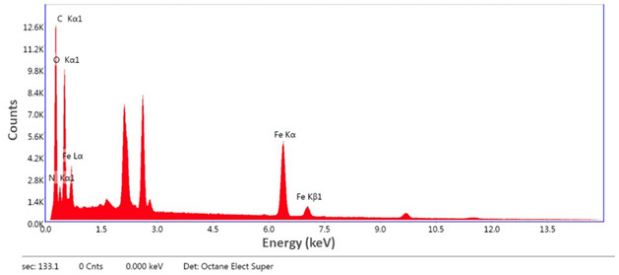

Figure 2. EDX spectra of MCH showing % composition of elements present in MCH.

The EDX spectra of MCH is shown in **Figure 2**, which clearly shows the successful incorporation of magnetite in pristine chitin. The percentage composition of Iron, Carbon, Nitrogen and Oxygen are found to be 40.58, 34.30, 6.34 and 18.78 wt.% respectively.

3.3 VSM analysis

From **Figure 3**, it is seen that magnetization (M) shows an increasing trend with applied magnetic field (H) and an *S* shaped hysteresis curve is obtained at 300 K for MCH. The zero coercivity and permanence in our samples indicate that the samples are superparamagnetic in nature. Low values of saturation magnetization were obtained in our sample. Rathinam *et al.*[26] have also reported a similar reduction in the value of saturation magnetization.

3.4 Thermogravimetric analysis (TGA)

The TGA curve of MCH as shown in **Figure 4** revealed a multistep decomposition pattern on heating to 900 °C in contrast to two steps degradation seen in pristine CH[27]. The evaporation of water is responsible for a slow and small weight loss of

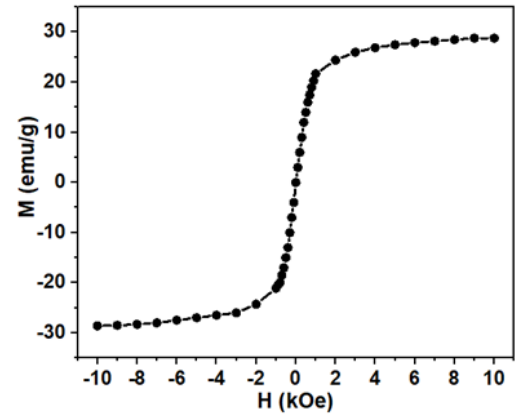

Figure 3. *S* shaped hysteresis curve showing superparamagnetic nature of MCH.

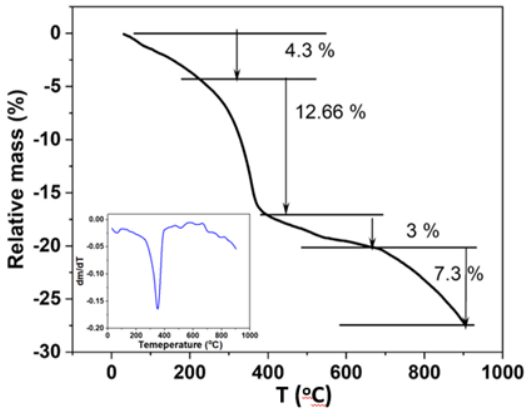

Figure 4. TGA curve of MCH showing multi step degradation at 800 °C.

4.3% from room temperature to 223 °C. At 350 °C, the maximum degradation occurs (shown in inset) wherein a weight loss of 12.66% is observed, due to the decomposition of polysaccharides. Beyond 400 °C, MCH shows a slow and steady weight loss of 3% until 665 °C. From 665 to 900 °C, the weight loss is however steeper at 7%. It is important to note that in pristine CH samples much higher weight loss is reported[28,29]. This clearly shows that MCH is thermally much stabler in comparison to pristine CH due to addition of magnetic nanoparticles. The percentage of residual mass at 800 °C in MCH is about 73%, which is significantly higher in comparison to pristine CH.

3.5 Complex impedance spectroscopy

The spectroscopic behaviour of complex impedance Z ($Z' + jZ''$) is plotted in **Figure 5** and **Figure 6** in the frequency range of ~1 Hz to 10 MHz respectively at select discrete temperatures ~300–400 K. The real part (Z') of the complex impedance represents resistive nature and the imaginary part

(Z'') represents the capacitive nature of the sample.

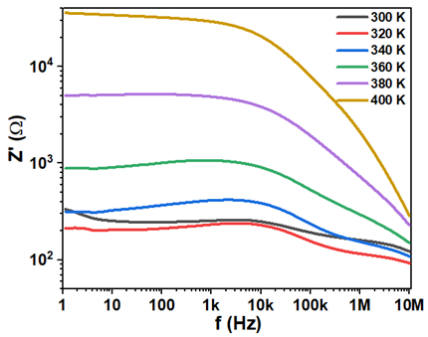

Figure 5. Plot of real impedance Z' versus frequency f.

From **Figure 5**, we see that qualitatively Z' decreases with increase in frequency indicating an improvement in electrical conductivity at high frequencies. It shows a plateau-like region at low frequencies, followed by a decrease at higher frequencies. The plateau region becomes predominant with increasing temperature, suggesting a strengthened relaxation behaviour. After this plateau region, Z' decreases with frequency (negative slope). This behaviour becomes more pronounced as the temperature increases. The decrease in Z' with frequency indicates relaxation processes in the system. The magnitude of Z' shows an increase with temperature, which is characteristic of a metallic behaviour[30]. The impedance values of our sample showed a decrease by more than two orders of magnitude with frequency at temperatures exceeding 340 K which may be attributed to the thermal activation mechanism.

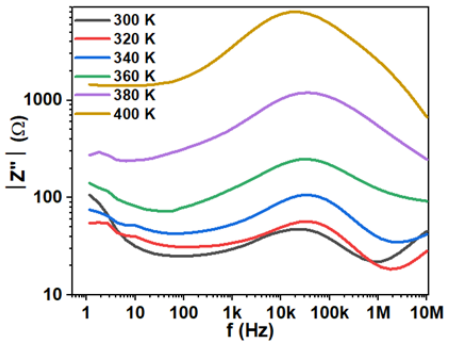

Figure 6. Plot of imaginary impedance Z'' versus frequency f.

From **Figure 6**, we see that the Z'' value increases initially, reaches a maximum value (Z''_{max}) at a specific frequency called the electrical relaxation frequency or characteristic frequency and then decreases continuously. As the temperature increases, a slight shift in the peak position towards smaller frequency is also observed, indicating change in relaxation time (τ). The change in position and broadness of the peaks with temperature indicates a thermally activated relaxation mechanism in our sample[14,31]. Utilizing this feature, we calculated the activation energy Ea in the following manner.

The frequency at which the impedance is maximum (Z''_{max}) is denoted by fmax from which relaxation time $\tau_{max}(= 1/f_{max})$ may be obtained. Then using the Arrhenius law $\tau_{max} = \tau_0\ exp(Ea/kbT)$, activation energy E_a may be estimated from the slope of the $ln(\tau_{max})$ versus $1/T$ graph[32]. Here τ_0 is a pre-exponential factor, k_b is the Boltzmann constant. **Figure 7** shows the plot $ln(\tau_{max})$ versus $1000/T$. Here a multiplier of 1000 to $1/T$ is used for numerical ease and adjusted in final calculation of the activation energy. From the slope, E_a is found to be 35.85 meV in the temperature range of 320 to 400 K.

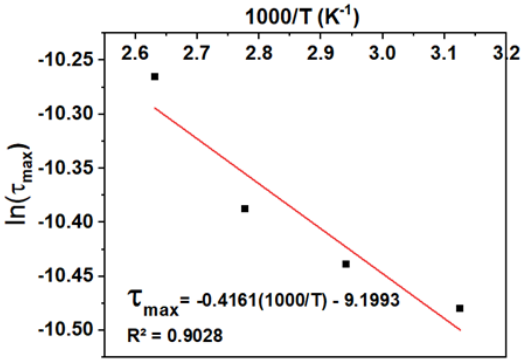

Figure 7. Arrhenius plot of $ln(\tau_{max})$ versus $1000/T$ for the calculation of activation energy E_a.

3.5.1 Nyquist plots

Figure 8 shows the Nyquist plots of the MCH at various temperatures. It is clearly visible that the plots are resolving towards better semicircular arcs with rise in temperature. The improvement in semicircular arc may be due to the restructuring of the grain boundaries[32,33] as the temperature increases. This is also suggestive of increase in the relaxation time and decrease in conductivity with temperature.

The shape of the Nyquist plot suggests an RC circuit equivalent with the peak of the semi-circle fulfilling the relation $\omega\tau_{max} = 1$. Here R, the parallel resistance in the RC equivalent circuit, can be determined from the Z'-span of the Nyquist plot. Since $\tau_{max} = 1/RC$, an estimate of capacitance C can be made. In our case, it was found to be in the range of 10^{-7} to 10^{-9} Farad, which is indicative of the

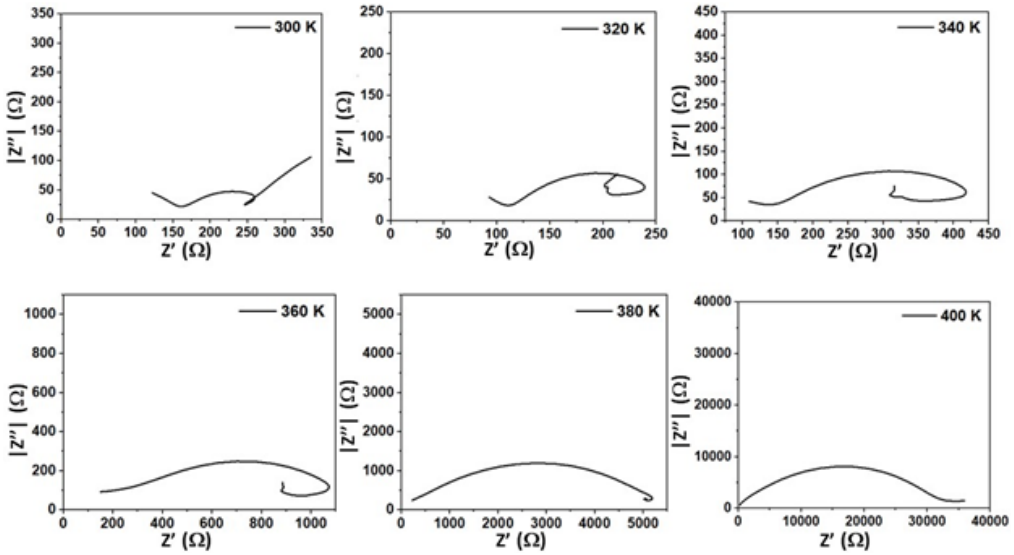

Figure 8. Nyquist plots of MCH at various temperatures.

involvement of surface layers. However, for a better understanding of this, it is more appropriate to use the detailed fitted data on capacitance from the dielectric measurements. This is done later in Section 3.6.

3.6 Dielectric properties

3.6.1 Complex permittivity

Figure 9 and **Figure 10** show the plots of the real permittivity ε' and the imaginary permittivity ε'' versus frequency (f) at different temperatures for our sample. The ε' values are quite high (>108 at 300 K) at low frequency—indicative of Maxwell Wagner type interfacial polarization in accordance with Koop's phenomenological theory[34,35], and show a decrease with increasing frequency for all temperatures. This is in agreement with the trends reported by other researchers in the field[31,36–38]. As the frequency increases appreciably, ε' also decreases appreciably due to decrease of the mentioned polarizations[14]. It is important to mention here that the permittivity observed in our sample is much higher than the permittivity reported in the pristine chitin sample[19,39]. It can be seen from **Figure 10** that loss peak is not present in the ε'' spectra, which is the characteristics of the charge carrier in the system. Further the plot of ε'' versus f on a log-log scale is a linear curve suggestive of DC conduction losses[40,41].

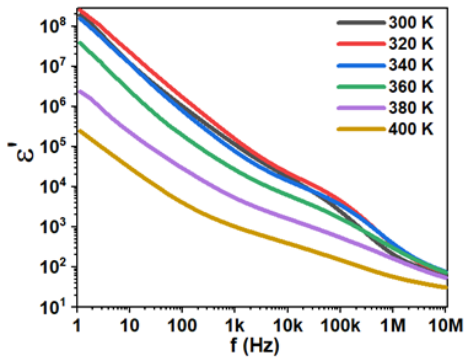

Figure 9. Plot of real permittivity ε' versus frequency f.

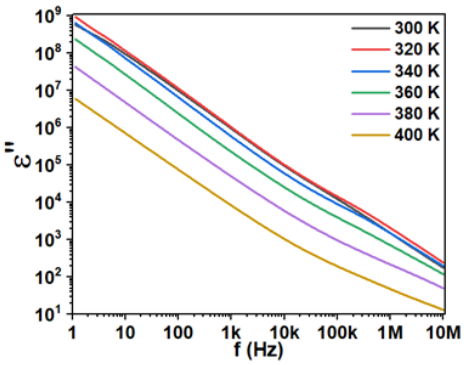

Figure 10. Plot of imaginary permittivity ε'' versus frequency f.

It can be seen from **Figure 9** and **Figure 10** that the rate of decrease of permittivity in the low frequency range is f^{-x} and tends to slow down to f^{-m} in the high frequency range. Both ε' and ε'' decrease almost similarly as f^{-x} in the low frequency range (ε': $0.9 \leq x \leq 1.2$ and ε'': $0.95 \leq x \leq 1.03$). So, we can conclude that both the components of the permittivity decrease linearly as almost f^{-1} in the low frequency range. However, at higher frequencies,

m was found to vary more significantly with temperature in both the cases. This information is used in determining the height of potential barrier from ε'' data. It is reported that $\varepsilon'' \propto f^{-m}$ where $0.57 \leq m \leq 0.90$. Let $\varepsilon'' = bf^{-m}$. Now $m = 4k_bT/w_m$[42], where T is temperature in Kelvin and w_m is the height of the potential barrier. Thus, by plotting m versus T in **Figure 11**, given below, we determined the height of potential barrier w_m as 95.8 ± 0.3 meV.

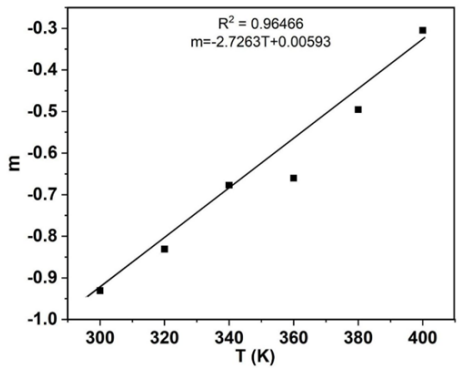

Figure 11. Plot of slope m versus T for the calculation of the height of potential barrier w_m.

Since the permittivity of any material is a measure of its polarizability, the data on real permittivity (ε') can be used to calculate the capacitance through the following relation.

$$\varepsilon' = \frac{Cd}{S\varepsilon_0},$$

where C is the capacitance of the sample, d is thickness, S is the area and ε_0 is the permittivity of vacuum/free space. Using this relation, we calculated capacitance C from the spectroscopic data on ε' at different temperatures. **Figure 12** illustrates the plot of C with frequency f on log-log scale at different temperatures.

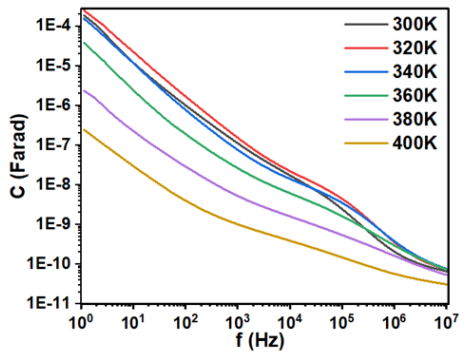

Figure 12. Plot of capacitance (C) versus frequency f.

From the above, it may be noted that C decreases with frequency. This dispersion relation between C and the power law of the form $C = af^{-x}$ ($0.392 \leq x \leq 0.932$) as shown in **Table 1**.

Table 1. Power exponent x and R^2 values at different temperatures for the capacitance versus frequency curves.

T (K)	*x*	R^2
300	0.932	0.9948
320	0.938	0.9951
340	0.882	0.9886
360	0.781	0.9809
380	0.498	0.9994
400	0.392	0.9956

It can be seen that from 300 to 320 K, C varies f^{-1} and thereafter it starts deviating from this f^{-1} dependence significantly. In other words, the dispersion of C decreases as T increases. This stability in frequency response of C at high temperature may be exploited in many such applications where dispersion needs to be minimal. Further it may be noted that the magnitude of the capacitance C lies in the range of 10^{-5} to 10^{-11} Farad for the frequency range of 1 Hz to 10 MHz studied by us. The variation in C with frequency can be broadly divided into three regions.

Region I: 10^{-4}–10^{-7} Farad attributable to sample-electrode interface and chemical reaction in the low frequency region of the graph.

Region II: 10^{-7}–10^{-9} Farad attributable to surface layers in the mid frequency region of the graph.

Region III: 10^{-9}–10^{-11} Farad in the high frequency region due to grain boundaries.

The contribution due to grain boundaries to the capacitance sets in at early frequencies as the temperature increases indicating grain restructuring as the temperature increases.

3.6.2 Dielectric loss

The interfacial polarization, DC conduction and molecular dipole movement contribute to the occurrence of dielectric loss of materials[43]. With increase in temperature, lattice vibrations and interactions between phonons and more mobile charge carriers increase, resulting in a high value of dielectric loss. The decrease in tangent loss. i.e., tan δ curve exhibits two loss peaks (**Figure 13**) which disappear with increase in temperature. A higher value of dielectric loss at high temperatures and low frequencies is observed and may be attributed

to charge accumulation and high resistivity at grain boundaries[32]. At temperatures of 360 K and above, the loss decreases rapidly up to 1 kHz while the rate of decrease is slow beyond 100 kHz. This behaviour is in conformity with the reported trends[44]. It is pertinent to note that the dielectric loss obtained in our sample is much esser than that reported by Badry *et al*. in Fe_3O_4/chitosan nanocomposite film[45]. It is observed that at frequencies higher than 10^5 Hz, the value of dielectric loss is minimum at temperatures exceeding 380 K.

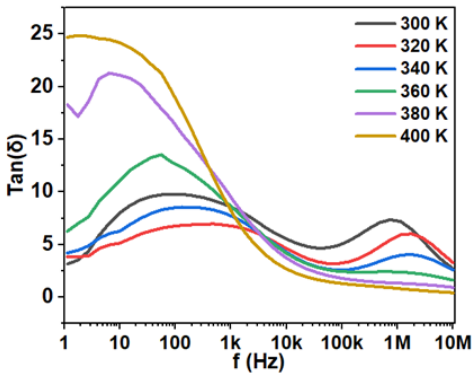

Figure 13. Dielectric loss tan (δ) versus frequency *f*.

4. Conclusions

In the presented work, we have successfully synthesized the magnetite-added chitin biopolymer as can be verified by XRD and EDX spectra reported by us. The synthesized sample exhibited superparamagnetism with an *S* shaped hysteresis loop with low values of saturation magnetization. MCH exhibited enhanced thermal stability and slow degradation in comparison to pristine chitin: a feature useful for many technological applications. The impedance curves indicate the presence of a single relaxation process. The activation energy E_a calculated from the impedance data is 35.85 meV in the temperature range of 320 to 400 K. The semicircular arcs obtained in Nyquist plots get better resolved with increase in temperature due to the restructuring of grain boundaries and are indicative of underlying RC equivalent circuit. Our sample showed strong insulating properties with a high dielectric constant at room temperature. The permittivity of MCH is reported to be higher than that of pristine CH. Both the dielectric permittivity and loss showed a marked reduction at high frequencies. The height of the potential barrier was determined to be 95.8 ± 0.3 meV from the permittivity data. The dispersion of estimated *C* decreases as *T* increases and the magnitude of *C* in different frequency regions are used to identify the mechanism behind it.

Acknowledgements

The authors are thankful to the Head of the Institution for his support and guidance.

Conflict of interest

The authors declare no conflict of interest.

References

1. Ahmetli G, Kocak N, Dag M, Kurbanli R. Mechanical and thermal studies on epoxy toluene oligomer-modified epoxy resin/marble waste composites. Polymer Composites 2012; 33(8): 1455–1463. doi: 10.1002/pc.22274.
2. Jayasree R, Chandrasekhar R, Cindrella L. Synthesis and characterization of polypyrrole-platinum composite for use as electrode material. Polymer Composites 2012; 33(9): 1652–1657. doi: 10.1002/pc.22285.
3. Bach VR, Zempulski DA, Oliveira LG, *et al*. Green synthesis of NiO nanoparticles and application in production of renewable H_2 from bioethanol. International Journal of Hydrogen Energy 2022; 47(60): 25229–25244. doi: 10.1016/j.ijhydene.2022.05.264.
4. Kumar MNVR. A review of chitin and chitosan applications. Reactive and Functional Polymers 2000; 46(1): 1–27. doi: 10.1016/s1381-5148(00)00038-9.
5. Hu X, Ricci S, Naranjo S, *et al*. Protein and polysaccharide-based electroactive and conductive materials for biomedical applications. Molecules 2021; 26(15): 4499. doi: 10.3390/molecules26154499.
6. Ikram R, Jan BM, Qadir MA, *et al*. Recent advances in chitin and chitosan/graphene-based bio-nanocomposites for energetic applications. Polymers 2020; 13(19): 3266. doi: 10.3390/polym13193266.
7. Safarzadeh M, Sadeghi S, Azizi M, *et al*. Chitin and chitosan as tools to combat COVID-19: A triple approach. International Journal of Biological Macromolecules 2021; 183: 235–244. doi: 10.1016/j.ijbiomac.2021.04.157.
8. Ndlovu SP, Ngece K, Alven S, Aderibigbe BA. Gelatin-based hybrid scaffolds: Promising wound dressings. Polymers 2021: 13(17): 2959. doi: 10.3390/polym13172959.
9. Babaei-Ghazvini A, Acharya B, Korber DR.

Antimicrobial biodegradable food packaging based on chitosan and metal/metal oxide bio-nanocomposites: A review. Polymers 2021; 13(16): 2790. doi: 10.3390/polym13162790.
10. Miao Y, Tan SN. Aerometric hydrogen peroxide biosensor based on immobilization of peroxidase in chitosan matrix crosslinked with glutaraldehyde. Analyst 2000; 125: 1591–1594. doi: 10.1039/B003483P.
11. Neubergera T, Schopf B, Hofmann H, *et al*. Superparamagnetic nanoparticles for biomedical applications: Possibilities and limitations of a new drug delivery system. Journal of Magnetism and Magnetic Materials 2005; 293(1): 483–496. doi: 10.1016/j.jmmm.2005.01.064.
12. Kaushik A, Khan R, Solanki PR, *et al*. Iron oxide nanoparticles–chitosan composite based glucose biosensor. Biosensors and Bioelectronics 2008; 24(4): 676–683. doi: 10.1016/j.bios.2008.06.032.
13. Kaushik A, Solanki PR, Ansari AA, *et al*. Iron oxide-chitosan nanobiocomposite for urea sensor. Sensors and Actuators B: Chemistry 2009; 138(2): 572–580. doi: 10.1016/j.snb.2009.02.005.
14. Kanagathara N, Sankar S, Saravanan L, *et al*. Dielectric and impedance spectroscopic investigation of (3-nitrophenol) -2,4,6-triamino-1,3,5- triazine: An organic crystalline material. Advances in Condensed Matter Physics 2022; 2022: 6002025. doi: 10.1155/2022/6002025.
15. Verma S, Mohanty S, Nayaka SK. Preparation of hydrophobic epoxy–polydimethylsiloxane–graphene oxide nanocomposite coatings for antifouling application. Soft Matter 2020; 16: 1211–1226. doi: 10.1039/C9SM01952A.
16. Kurahatti RV, Surendranathan AO, Kori SA, *et al*. Defence applications of polymer nanocomposites. Defence Science Journal 2010; 60(5): 551–563. doi: 10.14429/dsj.60.578.
17. Fu S, Sun Z, Huang P, *et al*. Some basic aspects of polymer nanocomposites: A critical review. Nano Materials Science 2019; 1(1): 2–30. doi: 10.1016/j.nanoms.2019.02.006.
18. Salaberria AM, Juanes RT, Badia JD, *et al*. Influence of chitin nanocrystals on the dielectric behaviour and conductivity of chitosan-based bionanocomposites. Composite Science & Technology 2018; 167: 323–330. doi: 10.1016/j.compscitech.2018.08.019.
19. Seoudi R, Nada AMA. Molecular structure and dielectric properties studies of chitin and its treated by acid, base and hypochlorite. Carbohydrate Polymers 2007; 68(4): 728–733. doi: 10.1016/j.carbpol.2006.08.009.
20. Movlaee K, Ganjali MR, Norouzi P, Neri G. Iron-based nanomaterials/graphene composites for advanced electrochemical sensors. Nanomaterials 2017; 7(12): 406. doi: 10.3390/nano7120406.
21. Gautam D, Lal S, Hooda S. Adsorption of Rhodamine 6G dye on binary system of nanoarchitectonics composite magnetic graphene oxide material. Journal of Nanoscience and Nanotechnology 2020; 20(5): 2939–2945. doi: 10.1166/jnn.2020.17442.
22. Tabuchi M, Ado K, Kobayashi H, *et al*. Magnetic properties of metastable lithium iron oxides obtained by solvothermal/hydrothermal reaction. Journal of Solid State Chemistry 1998; 141(2): 554–561. doi: 10.1006/jssc.1998.8018.
23. Liu Z, Wang J, Xie D, Chen G. Polyaniline-coated Fe_3O_4 nanoparticle–carbon-nanotube composite and its application in electrochemical biosensing. Small 2008; 4(4): 462–466. doi: 10.1002/smll.200701018.
24. Elsayed SA, El-Sayed IET, Tony MA. Impregnated chitin biopolymer with magnetic nanoparticles to immobilize dye from aqueous media as a simple, rapid and efficient composite photocatalyst. Applied Water Science 2022; 12: 252. doi: 10.1007/s13201-022-01776-3.
25. Holzwarth U, Gibson N. The Scherrer equation versus the 'Debye-Scherrer equation'. Nature Nanotechnology 2011; 6: 534. doi: 10.1038/nnano.2011.145.
26. Rathinam K, Jayaram P, Sankaran M. Synthesis and characterization of magnetic chitin composite and its application towards the uptake of Pb(II) and Cd(II) ions from aqueous solution. Environmental Pprogress & Sustainable Energy 2019; 38(1): S288–S297. doi: 10.1002/ep.13013.
27. Rogovina SZ, Alexanyan CV, Prut EV. Biodegradable blends based on chitin and chitosan: Production, structure, and properties. Journal of Applied Polymer Science 2011; 121(3): 1850–1859. doi: 10.1002/app.33477.
28. Shankar S, Reddy JP, Rhim JW, Kim HY. Preparation, characterization, and antimicrobial activity of chitin nanofibrils reinforced carrageenan nanocomposite films. Carbohydrate Polymers 2015; 117: 468–475. doi: 10.1016/j.carbpol.2014.10.010.
29. Jayakumar R, Selvamurugan N, Nair SV, *et al*. Preparative methods of phosphorylated chitin and chitosan—An overview. International Journal of Biological Macromolecules 2008; 43(3): 221–225. doi: 10.1016/j.ijbiomac.2008.07.004.
30. Koch CC. Nanostructured materials: Processing, properties, and applications. 2nd ed. Norwich:

William Andrew Publishing; 2007.
31. Triyono D, Supriyadi Y, Laysandra H. Investigation on electrical conductivity and dielectric property of $La_{0.8}Pb_{0.2}(Fe,Ti)_{0.5}O_3$ ceramic nanoparticles. Journal of Advanced Dielectrics 2019; 9(4): 1950029. doi: 10.1142/S2010135X19500292.
32. Rayssi C, Kossi SE, Dhahri J, Khirouni K. Frequency and temperature-dependence of dielectric permittivity and electric modulus studies of the solid solution $Ca_{0.85}Er_{0.1}Ti_{1-x}Co_{4x/3}O_3$ ($0 \leq x \leq 0.1$). RSC Advances 2018; 8: 17139–17150. doi: 10.1039/C8RA00794B.
33. Yan M, Jin J, Ma T. Grain boundary restructuring and La/Ce/Y application in Nd–Fe–B magnets. Chinese Physics B 2019; 28(7): 077507.
34. Koops CG. On the dispersion of resistivity and dielectric constant of some semiconductors at audio frequencies. Physical Review 1951; 83(1): 121–124. doi: 10.1103/PhysRev.83.121.
35. Chauhan L, Shukla AK, Sreenivas K. Dielectric and magnetic properties of Nickel ferrite ceramics using crystalline powders derived from DL alanine fuel in sol–gel auto-combustion. Ceramic International 2015; 41(7): 8341–8351. doi: 10.1016/j.ceramint.2015.03.014.
36. Batoo KM, Kumar S, Lee CG, Alimuddin A. Study of dielectric and ac impedance properties of Ti doped Mn ferrites. Current Applied Physics 2009; 9(6): 1397–1406. doi: 10.1016/j.cap.2009.03.012.
37. Soibam I, Phanjoubam S, Sharma HB, *et al*. Effects of cobalt substitution on the dielectric properties of Li–Zn ferrites. Solid State Communication 2008; 148(9–10): 399–402. doi: 10.1016/j.ssc.2008.09.029.
38. Thakur A, Mathur P, Singh M. Study of dielectric behaviour of Mn-Zn nano ferrites. Journal of Physics and Chemistry of Solids 2007; 68(3): 378–381. doi: 10.1016/j.jpcs.2006.11.028.
39. Chen H, Li X, Yu W, *et al*. Chitin/MoS_2 nanosheet dielectric composite films with significantly enhanced discharge energy density and efficiency. Biomacromolecules 2020; 21(7): 2929–2937. doi: 10.1021/acs.biomac.0c00732.
40. Jawad SA, Abu-Surrah AS, Maghrabi M, Khattari Z. Electric impedance study of elastic alternating propylene–carbon monoxide copolymer (*PCO*-200). Physica B: Condensed Matter 2011; 406(13): 2565–2569. doi: 10.1016/j.physb.2011.03.069.
41. Xi Y, Bin Y, Chiang C, Matsuo M. Dielectric effects on positive temperature coefficient composites of polyethylene and short carbon fibers. Carbon 2007; 45(6): 1302–1309. doi: 10.1016/j.carbon.2007.01.019.
42. Bouaamlat H, Hadi N, Belghiti N, *et al*. Dielectric properties, AC conductivity, and electric modulus analysis of bulk ethylcarbazole-terphenyl. Advances in Materials Science & Engineering 2020; 2020: 8689150. doi: 10.1155/2020/8689150.
43. Yang K, Huang X, Huang Y, *et al*. Fluoro-polymer@$BaTiO_3$ hybrid nanoparticles prepared via RAFT polymerization: Toward ferroelectric polymer nanocomposites with high dielectric constant and low dielectric loss for energy storage application. Chemistry of Materials 2013; 25(11): 2327–2338. doi: 10.1021/cm4010486.
44. Farid MT, Ahmad I, Aman S, *et al*. Structural, electrical and dielectric behavior of $Ni_xCo_{1-x}Nd_yfe_{2-y}O_4$ nano-ferrites synthesized by sol-gel method. Digest Journal of Nanomaterials and Biostructures 2015; 10(1): 265–275.
45. Badry MD, Wahba MA, Khaled RK, Farghali A. Preparation and dielectric properties of magnetite/chitosan nanocomposite film. Middle East Journal of Applied Sciences 2015; 5(4): 940–944.